JOURNAL OF BIOMEDICAL OPTICS 3(1), 66–75 (JANUARY 1998)

RESTORATION OF OPTICAL COHERENCE IMAGES OF LIVING TISSUE USING THE CLEAN ALGORITHM

Joseph M. Schmitt
Hong Kong University of Science and Technology, Department of Electrical and Electronic Engineering, Clear Water Bay, Kowloon, Hong Kong

(Paper JBO/IB-002 received July 9, 1997; revised manuscript received Sep. 3, 1997; accepted for publication Sep. 26, 1997.)

ABSTRACT

CLEAN, an iterative point-deconvolution algorithm developed originally for use in radio astronomy, was investigated as a means of restoring optical coherence tomography (OCT) images of biological tissue. The CLEAN deconvolution kernel was derived from the theoretical point-spread function of an OCT scanner, which depends on the properties of the imaging system as well as the characteristics of the scattering properties of the medium. The kernel incorporates a modification based on an inverse Wiener filter that is designed to reduce ripple artifacts in images of densely packed scatterers. Evaluation of the performance of the CLEAN algorithm was carried out on a set of images acquired with a prototype scanner with built-in speckle-reduction hardware. The results show the ability of the algorithm to improve the resolution of features in coherence images of scattering phantoms and living tissue. In many cases, the restored images reveal tissue morphology not evident in the unprocessed images. CLEAN tolerates speckle noise well and its performance degrades gracefully as the number of unresolvable scatterers causing mutual interference increases. Ways of coping with the long processing time required for the restorations are outlined, along with possible improvements that would permit CLEAN to take advantage of both amplitude and phase information in partially coherent interference signals. [S1083-3668(98)00301-3]

Keywords interferometry in biomedicine; optical coherence tomography; deconvolution; tissue optics interferometry; CLEAN.

1 INTRODUCTION

In clinical medicine, the tissue biopsy is the gold standard for definitive diagnosis of cancer and other pathological conditions. The possibility of noninvasive assessment of tissue pathology via an optical biopsy has been suggested recently by many investigators.[1–3] Optical coherence tomography (OCT),[4] a new technique that provides images of the subsurface morphology of living tissues, has a number of features that make it an attractive candidate for this application. OCT exploits the short temporal coherence of broadband light sources to achieve precise optical sectioning of highly scattering tissue in the depth dimension. Assembled using inexpensive components developed originally for the fiber-optic telecommunications industry, OCT scanners can image living tissue to depths of 1 to 2 mm with a resolution of 10 to 15 μm. Early results have encouraged researchers to explore the ability of OCT to guide, augment, or perhaps even replace conventional invasive biopsy procedures.[5–8]

Its considerable potential notwithstanding, OCT as currently implemented is unable to resolve subtle differences in subcellular morphology visible in stained histological sections. As a noninvasive imaging technique, OCT relies on the inherent differences in the refractive indices of tissue constituents to provide contrast. Thus it cannot take advantage of the selective staining techniques applied in conventional histopathological examinations. Because OCT employs heterodyne detection, it is susceptible to random interference between waves backscattered by nonresolvable scatterers. Such interference produces speckle noise that degrades contrast and resolution. Adding to these problems is the loss of coherence of the focused beam as it penetrates the tissue, which limits the maximum depth at which images can be obtained.

Progress has been made recently toward the solution of these problems in the design of OCT scanners. Reducing the temporal coherence of the light source and increasing its power have been shown to improve axial resolution and contrast, while providing a modest increase in penetration depth.[9,10] For reduction of speckle noise, an angular-diversity technique has been demonstrated using an array of detectors.[11] In principle, the techniques of adaptive optics[12] can be used to reduce blurring caused by

Address all correspondence to Joseph M. Schmitt. Tel: (852)2358-8515; Fax: (852)2358-1485; E-mail: eeschmit@ee.ust.hk

1083-3668/98/$10.00

wavefront aberrations. Nonetheless, before the full advantages of these advances can be realized, many technological constraints must be overcome. Even if their feasibility can be demonstrated successfully, some hardware solutions may be too expensive to apply in practice.

If present technological constraints are accepted, processing of the interference signals measured by OCT scanners is the only alternative strategy for improving image quality. Earlier studies have shown that simple depth-dependent gain techniques similar to those used in A-mode ultrasound can reduce the effects of attenuation on the appearance of optical coherence images.[13] Conventional spatial averaging filters, such as median and geometric filtering, can reduce speckle noise at the expense of image blurring.[14,15] However, these methods do nothing to replace the loss of information that results from convolution and mutual interference of the scattered beam. A deconvolution procedure that incorporates prior information about the point-spread function (PSF) of the OCT scanner is potentially a more effective basis for image restoration. The results of recent studies suggest that deconvolution can improve the resolution of highly reflecting objects in OCT images.[16,17]

In this study I investigated an iterative deconvolution algorithm, called CLEAN, whose effectiveness has been shown in radio astronomy, synthetic-aperture radar imaging, and lidar.[18–22] Among the attributes of this algorithm that make it attractive for deconvolution of optical-coherence images are its simplicity, stability in the presence of speckle noise, and ability to restore nonstationary signals. This paper begins by presenting a simple analytical form of the point-spread function of an OCT scanner that forms the basis of the kernel of the CLEAN algorithm. Then a simple modification is introduced to improve stability in the presence of noise. The effectiveness of the algorithm is evaluated on images acquired by a prototype OCT scanner that employs array-detection techniques.

2 THEORY

2.1 POINT-SPREAD FUNCTION OF AN OCT SCANNER

The point-spread function of an OCT scanner depends chiefly on two variables: the coherence function of the light source and the effective aperture of the interferometer. The source emission spectrum defines the coherence function, while the aperture is determined primarily by the pupil functions of the source and detection optics. However, because the effective aperture is also affected by the probing depth and the optical properties of the tissue medium, the PSF is not stationary in a general imaging context. Nevertheless, by making a few approximations that are not overly restrictive, it is possible to express the ensemble-averaged PSF as a simple function with a weak dependence on probing depth. With the PSF expressed in this way, its influence on image quality can be analyzed by using conventional linear systems theory.

Consider a point scatterer placed at the focus of the objective lens (focal length f) in the sample arm of the interferometer of an OCT scanner. A Gaussian beam ($1/e$ radius$=R$) illuminates the interferometer. The PSF is defined as the functional dependence of the interference signal on a small displacement Δr of the scatterer in the radial direction or Δz in the axial direction.

First suppose that multiple scattering in the medium is negligible. If the optical path matchpoint lies in the focal plane and the scattering of the light within the intervening space is neglected, the normalized single-scattered response can be written in the Gaussian approximation as[23]

$$h_s(\Delta r,\Delta z)=\exp(-\Delta z^2/l_c^2)\exp(-\Delta r^2/a_s^2)\cos\left[2k\Delta z + \frac{2k}{L}(\Delta r)^2\phi+2\tan^{-1}\left(\frac{2z_0\Delta z}{fL}\right)\right], \quad (1)$$

with

$$k=2\pi n/\bar{\lambda}, \quad z_0=kR^2$$

$$L=f-\Delta z, \quad l_c=\frac{0.44\bar{\lambda}^2}{n\Delta\lambda}$$

$$a_s^2=R^2[(L/z_0)^2+(\Delta z/f)^2]$$

$$\phi=[1-z_0^2\Delta z/Lf^2][1+z_0^2\Delta z^2/L^2f^2]^{-1},$$

where $\bar{\lambda}$ and $\Delta\lambda$ are the center wavelength and bandwidth of the source, respectively, and n is the refractive index of the medium. Random variations in the phase of the cosine term in Eq. (1) are responsible for the speckle noise evident in OCT signals generated by multiple scatterers within the sample volume.

Now consider multiple scattering, which spreads and attenuates the focused beam. If all of the incident light is assumed to scatter in the forward direction over small angles, multiple scattering can be accounted for by expressing the PSF as

$$h(\Delta r,\Delta z;z_d)=\exp(-\mu_s z_d)h_s(\Delta r,\Delta z)+(a_s^2/a_m^2)\times[1-\exp(-\mu_s z_d)]h_m(\Delta r,\Delta z), \quad (2)$$

which is a weighted sum of the single-scatter PSF in Eq. (1) and a multiple-scatter PSF, evaluated at a depth z_d in the medium,

$$h_m(\Delta r,\Delta z)=\frac{\sqrt{2}}{2}\exp(-\Delta z^2/l_c^2)\exp(-\Delta r^2/a_m^2). \quad (3)$$

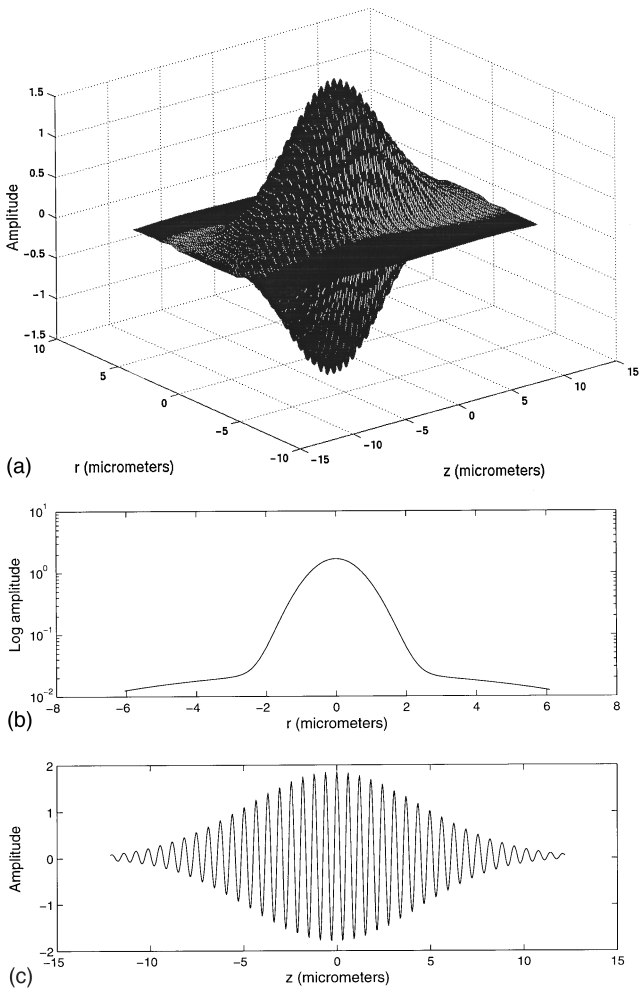

Fig. 1 Theoretical point-spread function of an OCT scanner from Eq. (1) of the text. (a) Two-dimensional view; r and z denote the radial and axial dimensions, respectively. (b) Radial slice of the envelope of the PSF plotted on a semilogarithmic scale ($z=0$). (c) Axial slice of the PSF ($r=0$). In this example, the variables that determine the shape of the PSF were set as follows: $f=12$ mm, $R=2.4$ mm, $\bar{\lambda}=1.3$ μm, $z_d=500$ μm, $\Delta\lambda=80$ nm, $\theta_{\rm rms}=6°$, $n=1.38$, $\mu_s=8$ mm^{-1}.

This expression is similar to Eq. (1), except the cosine term has been set to its average value, $\sqrt{2}/2$, and the radial width a_s^2 has been replaced by the depth-dependent function

$$a_m^2=R^2\left[(L/z_0)^2+(\Delta z/f\,)^2+\frac{\mu_s z_d L^2\theta_{\rm rms}^2}{3R^2}\right], \quad (4)$$

which is the mean-square width of the backscattered beam, given by the sum of the widths of the diffraction-limited beam and the cone of the multiply forward-scattered light. The rms scattering angle, $\theta_{\rm rms}$, which depends on the distribution of particle sizes, can be estimated from the half-width of the forward lobe of the single-scattering phase function of the medium.[23]

Equation (2) is plotted in Figure 1 for a set of input variables that model an OCT scanner focused 500 μm deep in a tissue medium. For this example, the modeled scattering properties of the medium ($\mu_s=8$ mm^{-1}; $\theta_{\rm rms}=6$ deg) were chosen to represent those of the dermis. The central Gaussian peak in the radial profile of the PSF plotted in Figure 1(a) corresponds to the single-scatter (diffraction-limited) component of the PSF, and the slightly curved baseline on which it lies corresponds to the multiple-scatter component. As pointed out earlier, the PSF given by Eq. (2) is nonstationary because it depends not only on Δr and Δz, but also on the probing depth. However, because $a_m^2 \gg a_s^2$ for normal imaging conditions in tissue at depths exceeding a few hundred micrometers, the PSF can be approximated as a quasi-stationary function,

$$h(\Delta r,\Delta z)\sim\exp(-\mu_s\bar{z})h_s(\Delta r,\Delta z)+c_0 \quad (5)$$

where $\exp(-\mu_s\bar{z})$ is the mean loss factor and $c_0=a_s^2/a_m^2(\bar{z})=(1+\mu_s z_0^2\bar{z}/3R^2)^{-1}$ is the mean amplitude of the multiple-scatter PSF, both evaluated at a depth $\bar{z}$ in the middle of the scan range. This simplified form of the PSF is based on the assumption that the sizes of the scatterers are too small to cause refractive distortion of the shape of the main lobe and therefore simply attenuate the beam by dispersing it at wide angles.[23] It follows that Eq. (5) is not valid for a medium characterized by large-range correlations in the refractive index structure. In practice, correction for loss of single-backscattered light can be accomplished in real time during image acquisition by using a variable-gain amplifier that functions like the time-gain compensation circuits employed in ultrasound scanners.

It is important to realize that the ensemble-averaged PSFs given by Eqs. (2) and (5) are valid in an average sense only, because these expressions do not account explicitly for the random nature of beam propagation through the refractive index heterogeneities in tissue.

2.2 ITERATIVE POINT DECONVOLUTION

Armed with an estimate of the point-spread function of the OCT scanner, we can now apply this knowledge to the solution of the estimation problem that underlies the reconstruction of optical coherence images.

Suppose that a tissue is composed of a collection of M point scatterers with different backscattering coefficients. The object distribution, which is the distribution (image) that we wish to reconstruct, is then

$$o(r,z)=\sum_{i=1}^{M}\sigma_{b,i}\delta(r-r_i,z-z_i) \quad (6)$$

where r_i and z_i are the coordinates of the i'th scatterer and $\sigma_{b,i}$ is its backscattering coefficient. It fol-

lows from the definition of the PSF in linear systems theory that the image of the object distribution is

$$s(r,z)=\sum_{i=1}^{M} o(r_i,z_i)h(r-r_i,z-z_i)+n(r,z) \quad (7)$$

or, equivalently, in convolution form,

$$s(r,z)=o(r,z)**h(r,z)+n(r,z). \quad (8)$$

The term $n(r,z)$ in these equations represents the noise introduced by the measurement process. The fundamental problem is to derive the best estimate of $o(r,z)$ from $s(r,z)$. If the Fourier transform of $h(r,z)$ has no zeros and the noise introduced by the measurement process is negligible, $o(r,z)$ can be recovered simply by dividing by a matched filter in the Fourier domain and then inverse Fourier transforming the result according to

$$o(r,z)=\mathcal{F}^{-1}\left(\frac{S}{H}\right) \quad (9)$$

where S and H are the 2-D Fourier transforms of the image function and PSF, respectively, and $\mathcal{F}^{-1}$ denotes inverse Fourier transformation. Unfortunately, in practical OCT systems, H approaches zero rapidly as the spatial frequency approaches the limit set by the bandwidth of the source (in the axial direction) and the effective aperture of the lens (in the lateral direction), making the ratio unstable in the presence of noise. The CLEAN algorithm, outlined in the next section, provides a more robust means of deconvolving the PSF from measured OCT data.

2.3 THE CLEAN ALGORITHM

Unlike conventional deconvolution methods based on the Fourier transform, CLEAN is an iterative nonlinear algorithm that operates in the spatial domain. CLEAN has been applied extensively in optical and radio astronomy and has been shown to work well for processing speckled images, even when the optical-transfer function of the imaging system contains wide gaps in which the spatial frequency response is close to zero.[24]

The basic steps in the CLEAN algorithm are as follows: (1) Create a zeroed 2-D array to hold the deconvolved image (the ''clean'' image). (2) Find the coordinate (r',z') of the brightest pixel in $i(r,z)$, the original image (the ''dirty'' image). (3) Subtract a fraction of the deconvolution kernel $\alpha h(r-r',z-z')[s(r',z')/h(0,0)]$ from the $s(r,z)$, where α is the loop gain, with a value less than 1. (4) Add the quantity $\alpha i(r',z')$ to the pixel of the clean image at coordinate (r',z'). (5) Repeat steps (2 to 4) until the maximum value in the dirty image falls below the noise floor. (6) After the iterations are finished, convolve the clean image with a smooth function having a spatial extent chosen to interpolate between adjacent delta functions.

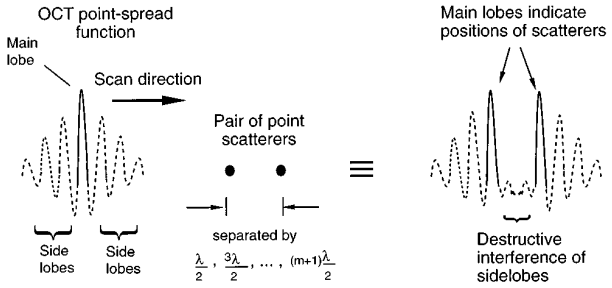

Fig. 2 Interaction of the ''main lobes'' and ''side lobes'' of the point-spread function of an OCT scanner with a pair of point scatterers. Convolution with scatterers separated by an odd multiple of the wavelength leads to destructive interference of the side lobes, but not the main lobes. The locations of the peaks of the convolved main lobes in the interference signal correspond to the locations of the scatterers. The CLEAN algorithm is designed to extract these peaks.

In the application of CLEAN in radio astronomy, the primary goal is to reduce artifacts generated by large side lobes in the response function of the receiving antenna array. Similar artifacts degrade optical coherence images, but the interpretation of their origin is not as straightforward. In the terminology of antenna theory, the central peak of the single-scattered PSF in Eq. (1) is the ''main lobe'' of the OCT response function and the cosinusoidal oscillations in the axial response within the coherence window are the ''side lobes,'' which interfere and create artifactual signals that appear as speckle in images. It follows naturally from these rather unorthodox definitions that a hypothetical source with a coherence length less than $\lambda/2$ (a temporally incoherent source) would possess only a main lobe and would be incapable of generating speckle.

Figure 2 illustrates this concept for the special case of destructive interference between waves backscattered from two particles. If the features in the image that result from interaction of the target scatterers with the main lobe could be distinguished from those that result from interaction with the side lobes, then deconvolution and speckle reduction could be accomplished simultaneously. This is the rationale that motivated the present study of the CLEAN algorithm for deconvolution of optical coherence images. However, because the coherence lengths of sources used in OCT are typically 10 to 20 optical cycles long, the energy in the side lobes greatly exceeds that in the main lobe. Also, constructive interference can strengthen side lobes and cause the CLEAN algorithm to falsely identify a side lobe as a main lobe.

Simulations carried out in an earlier study indicate that the CLEAN algorithm is unable to extract the true object function from OCT images of dense tissue, because the deconvolution procedure amplifies the high-frequency fluctuations caused by

speckle.[17] For this reason, I chose to apply the CLEAN algorithm to a set of images acquired by an OCT scanner that suppresses speckle by combining views of a given sample volume taken from different angles (see Ref. 11 and the description in Sec. 3.1). This angular-diversity process reduces the speckle noise power and facilitates detection of the peak of the main lobe of the PSF of the scanner. As the experimental results presented in Sec. 4 show, the better signal-to-noise ratio of angular-diversity OCT images permits the CLEAN algorithm to operate more effectively.

2.4 MODIFICATION OF THE CLEAN ALGORITHM

A deficiency of the standard CLEAN algorithm is its inability to accurately reconstruct extended objects, i.e., objects composed of closely spaced scatterers. The standard CLEAN algorithm works best when target features are separated by distances greater than the width of the main lobe of the PSF. Reconstructions of extended objects tend to appear corrugated, because artifacts are created by incomplete subtraction of residuals. These artifacts, which are well recognized,[19,20] limit the utility of CLEAN in reconstructing images of tissues containing high densities of nonresolvable scatterers.

To bias CLEAN toward smoother reconstructions, I adopted an argument of Bates, Fright, and Bates[21] that is founded on the relationship between conventional Fourier inversion and CLEAN. These researchers argued that extended images ought to be CLEANed with a modified PSF equal to the inverse Fourier transform of the reciprocal of the Wiener filter. Written in its general form, the Wiener restoration filter is[25]

$$W=\frac{1}{H}\frac{\langle OO^{*}\rangle+0.5\langle O^{*}N\rangle+0.5\langle N^{*}O\rangle}{\langle OO^{*}\rangle+\langle O^{*}N\rangle+\langle N^{*}O\rangle+\langle N^{*}N\rangle} \quad (10)$$

where H and O are the Fourier transforms of the PSF and the object distribution, respectively, and N is the Fourier transform of the image noise. Assuming that the object distribution and the noise are uncorrelated, then the generalized Wiener filter in Eq. (10) simplifies to

$$W=\frac{1}{H}\frac{|O|^2}{|O|^2+|N|^2} \quad (11)$$

where $|O|^2=\langle O^{*}O\rangle$ and $|N|^2=\langle N^{*}N\rangle$ are the power spectral densities of the object distribution and the noise. According to Bates, Fright, and Bates, the optimum kernel for carrying out the CLEAN restoration is then

$$h'(r,z)=\mathscr{F}^{-1}\left\{\frac{1}{|W|}\right\}=|h(r,z)|+\mathscr{F}^{-1}\left\{|H|\,\frac{|N|^2}{|O|^2}\right\}. \quad (12)$$

Full evaluation of the second term of this expression requires prior knowledge of the power spectral densities of the object distribution (the ideal signal) and the noise. Such information is not, in general, available. Nonetheless, it is still possible to infer certain characteristics of the signal and noise from which an appropriate deconvolution kernel can be derived. To estimate the effect of the power spectral density of the noise on $h'(r,z)$, first consider the extreme case of fully developed speckle noise in which multiplicative noise dominates, so that $|N|^2=k|O|^2$, where k is a constant. In this case, the optimum cleaning kernel is

$$h'_s(r,z)=(1+k)|h(r,z)|, \quad (13)$$

which is simply a scaled version of the magnitude of the point-spread function. Therefore, no modification of the standard CLEAN algorithm is required to deal with optical coherence images corrupted by fully developed speckle. On the other hand, for images such as those considered in this paper in which speckle has been suppressed by using an angular-diversity technique, it is more appropriate to assume that a large fraction of the noise is additive and has a broad spectrum approximated by $|N|^2=$constant. The power spectral density $|O|^2$ is related to the sizes of structures in tissue, which range from a fraction of a micrometer to several millimeters. Although it would be desirable to image tissue elements within this entire range of dimensions, diffraction precludes the formation of images of structures substantially smaller than the width of the PSF. It seems reasonable then to narrow the definition of the *true* object distribution to the *resolvable* object distribution and choose $|O|^2\approx|H|$. Given this assumption, the optimum cleaning kernel can be written as

$$h'(r,z)\approx|h(r,z)|+k'\delta(r,z) \quad \text{for } |h(0,0)|=1, \quad (14)$$

where k' is a constant proportional to the mean amplitude of the additive white noise present in the acquired image. This kernel, which is composed of the theoretical PSF [Eq. (2)] and a superimposed delta function whose amplitude depends on the white noise amplitude, was used in the modified CLEAN restorations in this study. A similar kernel was introduced by Cornwell for stabilization of the CLEAN algorithm in restoration of radio-frequency interferograms.[19] In the limit $k'\to0$, the modified kernel reverts to the standard kernel, $h'(r,z)=|h(r,z)|$.

3 MATERIALS AND METHODS

3.1 OCT SCANNER

A prototype OCT scanner, described in detail in Ref. 10, was used to acquire a set of images for processing with the CLEAN algorithm. The scanner

uses free-space optics in each arm of a Michelson interferometer. An edge-emitting light-emitting diode (LED) (peak wavelengths $\lambda_p = 1.3\ \mu$m; full-width half-maximum (FWHM) bandwidth=45 nm; emission power=60 μW) coupled into a short length of a single-mode fiber serves as the light source. An aspheric objective lens (NA = 0.4, working distance=5.0 mm) and a miniature retroreflector are mounted together on a voice-coil scanning stage that is set up to perform constant-velocity scans. The movement of the retroreflector tracks the optical path to the focal plane of the lens dynamically. Acquisition of each 600 (depth)×400 (lateral)-pixel image requires about 20 s.

The detection optics of the scanner are designed to suppress speckle noise according to the principles of angular-diversity processing.[11] At the output of the interferometer, the sample and reference beams mix on the surface of an InGaAs quadrant photodiode. Images are formed from the sum of the photocurrents from the four detector elements after bandpass filtering and rectification. A time-variable gain amplifier synchronized with the axial movement of the stage amplifies the combined signal to compensate for the depth-dependent attenuation of the probe beam. In optical coherence tomography of dense tissue, this type of signal processing has been shown to increase the ratio of the signal and speckle noise powers by a factor of about 2, at the expense of slight blurring of the edges of image features.

3.2 IMAGE ACQUISITION AND PROCESSING

The performance of the CLEAN algorithm was evaluated on OCT images obtained from a tissue phantom and from skin tissue *in vivo*. The phantom consisted of a block of solid gelatin (30% protein by weight) in which polystyrene microspheres of two sizes were suspended. The larger-sized spheres (6 μm diameter), which were dispersed throughout the block in low concentration (0.2% by volume or approximately one particle for every 7 sample volumes), served as the target objects. With a concentration of 0.4% (more than 1000 particles per sample volume), the smaller-sized spheres (0.2 μm diameter) served as the background medium.

For the evaluation of the images of living tissue, OCT scans of the dorsal aspect of the index finger of an adult male were obtained by focusing the scanning objective through a hole in a rigid plate against which the finger was pressed. Before each scan was taken, a layer of glycerin was spread on the surface of the skin to reduce the phase aberrations caused by the rough tissue–air interface. The finger was held as still as possible during the scan, but was not fixed rigidly to the plate.

The standard and modified versions of the CLEAN algorithm were applied to deconvolve the rectified interference signals in two dimensions. The images were processed off-line using the algorithms outlined in Sections 2.3 and 2.4. The positive magnitude of the theoretical PSF [Eq. (2)] served as the CLEAN deconvolution kernel, with the following constants used to define $|h(\Delta r, \Delta z)$: $f = 12$ mm, $R = 1.5$ mm, $\bar{\lambda} = 1.3\ \mu$m, $\Delta\lambda = 45$ nm, $n = 1.38$, $\theta_{\text{rms}} = 8°$, $\mu_s = 8\ \text{mm}^{-1}$. As specified by Eq. (14), a delta function (one pixel wide), was added to $|h(\Delta r, \Delta z)|$ in the modified CLEAN deconvolutions. All of the negative residuals were set equal to 0.

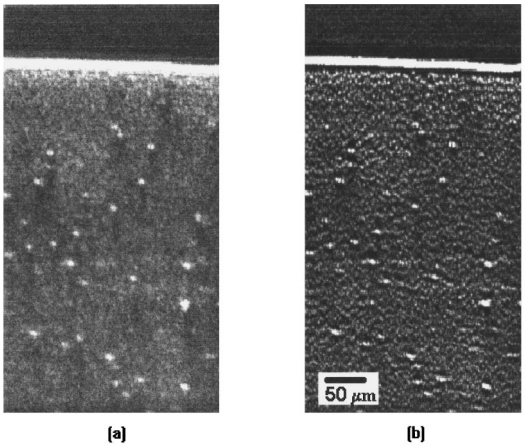

Fig. 3 Cross-sectional images of a gelatin tissue phantom containing 6 μm-diameter latex spheres in a background of densely concentrated 0.22-μm-diameter spheres. (a) Original speckle-reduced image. (b) Image after deconvolution using the modified CLEAN algorithm. The scale shown by the white bar applies to both the horizontal (lateral) and vertical (depth) dimensions. Both images are displayed on the same gray scale after square-root compression.

Iterations were stopped when the magnitude of the residuals in the dirty image fell below the root-mean-square shot-noise level, which was recorded with the tissue removed from the sample arm. After the clean images were formed, they were reconvolved with a two-dimensional Gaussian function having an FWHM of 6 μm in the lateral and depth dimensions. With the loop gain set equal to 0.25, the total processing time for a 600×400-pixel image was about 30 min on a Sun SPARC-20 workstation.

4 RESULTS AND DISCUSSION

4.1 PERFORMANCE ASSESSMENT: IMAGES OF TISSUE PHANTOMS

The cross-sectional images of a gelatin tissue phantom in Figure 3 illustrate the salient features of CLEAN deconvolution. Owing to the angular-diversity processing of the OCT signal, the 6-μm particles are easy to distinguish in the image before deconvolution [Figure 3(a)], in spite of the speckle noise generated by backscattering from the large number of subwavelength-diameter particles in the background. However, especially in the depth dimension, the spatial extent of the particle images is enlarged as a result of convolution with the PSF of the scanner. After deconvolution, the images of the

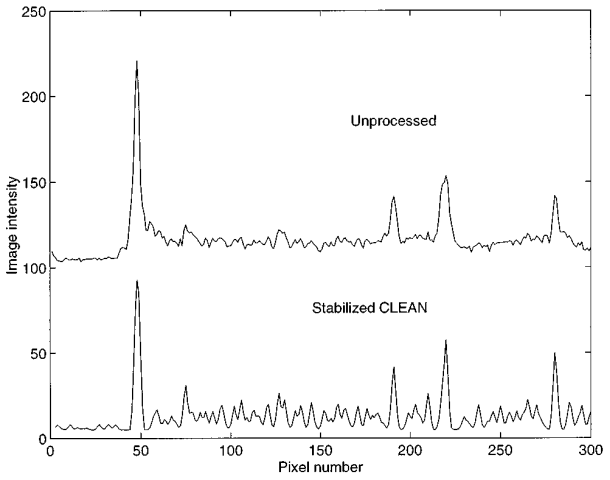

Fig. 4 Profiles taken from a vertical line that intersects three 6 μm-diameter spheres in the processed and unprocessed images of the tissue phantom in Figure 3. The centers of the spheres are located at pixel numbers 190, 219, and 281. Each pixel unit on the abscissa corresponds to about 2 μm of depth in the medium (assuming $n = 1.38$). To facilitate comparison, the top profile is offset by 100 from the profile immediately below it. The magnitudes of the profile data were compressed with the square-root function and scaled for display in the 0 to 100 range.

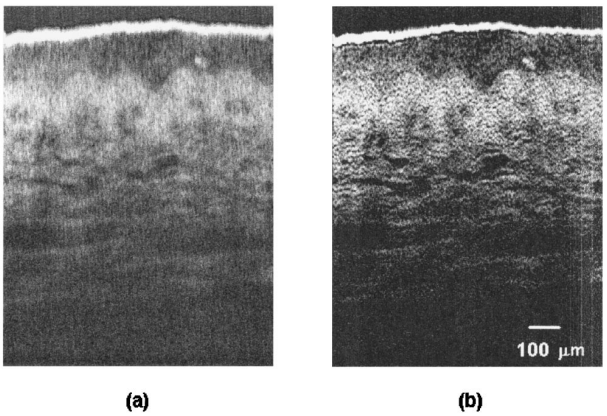

Fig. 5 (a) OCT image of the dorsal side of the skin of the index finger between the phalangeal joints. The speckle noise in this image has already been reduced by incoherent addition of signals from four detectors. (b) Image after deconvolution using the modified CLEAN algorithm. The surface of the skin is at the top of the image. The scale shown by the white bar applies to both the horizontal (lateral) and vertical (depth) dimensions. Both images are displayed on the same gray scale after square-root compression.

particles appear sharper and their dimensions are closer to their actual sizes, but the variance of the speckle noise in the background is substantially larger. These results illustrate a general characteristic of the CLEAN deconvolution procedure shared by other deconvolution methods: improvement in resolution comes at the expense of a loss in the signal-to-noise ratio (SNR).

The one-dimensional image profiles in Figure 4 illustrate the nature of the tradeoff between resolution and SNR. The selected profile, which was taken along a line in the depth dimension, cuts through the image of three particles which appear as isolated peaks in the profile. Compared with those in the unprocessed image profile, the peaks in the CLEANed profile are sharper and their full-widths at half-maximum are closer to the actual diameters of the particles. By measuring the widths of the edge responses of the particles, I found that CLEAN deconvolution improved resolution by a factor of 1.5 to 2.0. However, the SNR, defined here as the average magnitude of the peak signal intensity generated by backscattering from the 6-μm particle, divided by the variance of the background speckle noise generated by the 0.2-μm particles, decreased from an average of 85 to 44. Thus, according to these definitions, the factors by which CLEAN improved the resolution and degraded the SNR were similar.

The results of this experiment are consistent with those of Fried,[24] who pointed out that deconvolution in the coherent imaging context can be regarded as a kind of superresolution process that consumes excess SNR. In this experiment, the SNR of the deconvolved image was still large enough that visualization of the large particles was not significantly impaired. In a situation that requires imaging of a dense concentration of weakly backscattering objects, a loss in SNR of this magnitude could be unacceptable. Unfortunately, a quantitative measure of image quality that embodies the effects of resolution and SNR has not yet been worked out. Therefore, the appearance of unprocessed and processed images of tissue is still the standard by which the value of the CLEAN deconvolution in a particular application must ultimately be judged.

4.2 DECONVOLUTION OF TISSUE IMAGES

Figure 5 is an example of an OCT image of the skin of the index finger before and after restoration with the modified CLEAN algorithm. Enlarged views of the images are shown in Figure 6.

The stratum corneum appears in Figure 5(a) as a weakly backscattering layer just below the top surface and above the highly backscattering basal cell layer of the epidermis. The boundary between the stratum corneum and living epidermis is blurred by vertical streaks that extend 5 to 8 μm (about half the source coherence length) into the weakly backscattering region. The streaks are also evident throughout the epidermis. In contrast, the boundary appears sharp in the restored image [Figure 5(b)] and can be followed easily across the entire lateral dimension of the image.

As expected, blurring in the lateral dimension of the unrestored image is not as severe, because the width of the PSF in this dimension is narrower. However, because the angular-diversity technique used by the scanner to suppress speckle noise reduces the effective aperture,[11] the PSF of the scan-

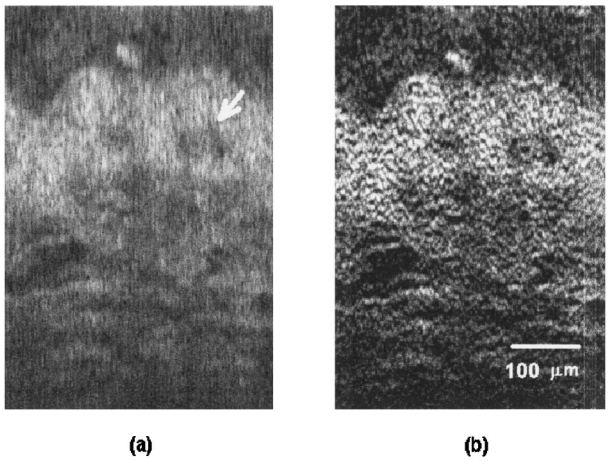

Fig. 6 Expanded views of an epidermal fold in the images in Figure 5. (a) Unprocessed image. (b) Image after modified CLEAN deconvolution. The scale shown by the white bar applies to both dimensions. The arrows mark the locations of the cross sections of a capillary loop. Note that the walls of the capillary on the right side are visible in the deconvolved image.

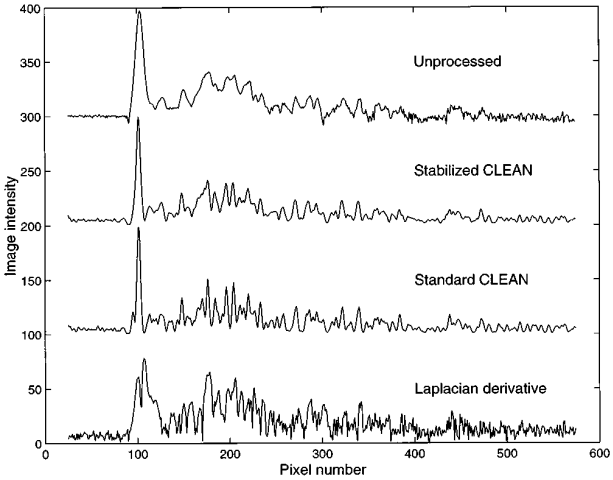

Fig. 7 Profiles taken from a vertical line (300th from the left) of the processed and unprocessed images of the skin in Figure 5. Each pixel unit on the abscissa corresponds to about 2.5 μm of depth in the medium (assuming $n = 1.38$). To facilitate comparison, each of the top three profiles is offset by 100 from the profile immediately below it. The magnitudes of the profile data were compressed with the square-root function and scaled for display in the 0 to 100 range.

ner is broader than the diffraction-limited PSF determined by the full numerical aperture of the lens. Since the deconvolution kernel used in the reconstructions accounted for this degradation in lateral focusing, the CLEAN algorithm attempted to sharpen the image in the lateral as well as the depth dimension. The improved clarity of isolated features in the image attests to the advantages of applying deconvolution in both dimensions. Consider, for instance, the circular cross sections of two capillaries marked by the arrows in the enlarged images in Figures 6(a) and 6(b). Although the internal structures of the capillaries are difficult to discern in the original image, the walls of at least one of the vessels can be distinguished in the restored image.

As mentioned in Sec. 2.4, one deficiency of the CLEAN algorithm is its tendency to produce rippling or corrugations in uniformly blurred regions of an image. The modified CLEAN algorithm alleviates this problem but does not eliminate it. A close comparison of Figures 6(a) and 6(b) reveals areas in which threadlike features are generated that may not correspond to the real structure. Residual multiplicative speckle noise or reflections from flat scatterers produce gaps in the interference signal that may promote the formation of such artifacts.

At the base of the dermis are horizontal fiber bundles through which larger blood vessels penetrate. The images of these structures, located at the bottom of Figure 5, appear dim because the magnitudes of the interference signals from which they were formed were small (<10 dB above the noise floor). In spite of the low signal-to-noise ratio, the deconvolution procedure appears to have sharpened the boundaries of the blood vessels without creating spurious reflections in the adjacent weakly backscattering (dark) regions.

The image profiles in Figure 7, which were taken along a vertical line of the image in Figure 5(a) after processing, illustrate the ability of the CLEAN algorithm to resolve superimposed peaks over a wide range of signal levels. The width of the peaks produced by an isolated scatterer (or group of scatterers) in the depth dimension were reduced by a factor of approximately 2, without significant amplification of high-frequency noise. Figure 7 also illustrates the lower noise sensitivity of the CLEAN deconvolution procedure compared with that of the conventional sharpening filter (the Laplacian derivative). Although both are effective in narrowing the peaks of strong signals produced by isolated scatterers, the conventional sharpening filter accentuates small-amplitude variations caused by high-frequency noise.

In contrast, the standard and modified CLEAN algorithms attenuate rather than amplify noise variations (compare the segments of profiles between pixels 400 and 570). Compared with the standard CLEAN algorithm, the modified CLEAN algorithm smooths high-frequency noise better and tracks the density of scatterers more faithfully in regions where the scatterers are packed too closely for deconvolution to be effective (compare the segments of the profiles between pixels 125 and 325, which were taken from the images of the densest part of the epidermis). These results suggest that the CLEAN restoration procedure behaves as a differentiator combined with a bandpass filter that adapts to the local spectral density of the signal.

I found the CLEAN algorithm to perform equally well on images of skin acquired from other regions of the body with the same scanner. In all cases, structures in the restored images appear sharper and easier to distinguish from adjacent structures.

4.3 SENSITIVITY TO INPUT VARIABLES

How sensitive are CLEAN restorations of coherence images to the variables that define the shape of the point-spread function and control the convergence of the iterative point deconvolution? Since CLEAN is a nonlinear algorithm, it is difficult to analyze these sensitivities analytically. As an alternative, I examined the results of a set of restorations of a group of images to study the effects of different variables. My observations are summarized below as a set of guidelines.

1. The variables that define the shape of the PSF (f, R, $\bar{\lambda}$, $\Delta\lambda$, θ_{rms}, and μ_s) used in the restorations should be chosen to match the characteristics of the scanner and the tissue medium as closely as possible. Whether the shape of the envelope of the main lobe of the PSF is modeled best as a Gaussian or similar smooth curve is not the principal concern; most important are its axial and radial widths. If the widths are set too large, ringing and other artifacts appear in the restored images; if they are set too small, the sharpness of the reconstruction diminishes. To satisfy the Nyquist criterion, at least two pixel elements must be fit within the smallest dimension of the main lobe of the PSF.

2. Provided that its value does not exceed about 0.5, the loop gain used in the CLEAN algorithm is not critical. A value of 0.25 gave good results for all of the images in the test set. Values smaller than about 0.1 did not improve the quality of the restorations. In restorations in which only the magnitudes of the positive-valued (rectified) interference signals are used, convergence can be made faster if negative residuals are set to zero. The CLEAN algorithm tolerates a wide range of noise floor estimates as a stopping criterion for the iterations. Setting the noise floor a factor of 2 above or below the measured root-mean-square amplitude caused no noticeable changes in the restored images.

3. In the modified CLEAN algorithm, the amplitude k' of the 1-pixel-wide delta function superimposed on the main lobe of the deconvolution kernel mainly affects the smoothness of the reconstructions. In the present study, $k' = 0.5$ was found by trial and error to be a good choice for processing the images in the test set. Sharper images were obtained at the expense of higher-amplitude ringing artifacts and broadband noise by setting k' closer to zero; for $k' \gg 1$, smoothing of edges was apparent.

5 CONCLUSION

The results of this study show that the resolution and contrast of optical coherence images can be improved significantly by deconvolving the point-spread function of the OCT scanner. A modified version of the CLEAN algorithm appears to provide an effective way of improving resolution in optical coherence tomography. Although a reliable measure does not yet exist to quantify resolution in a medium as complex as tissue, the results suggest that the CLEAN procedure can narrow the cross section of the image of an isolated scatterer or group of scatterers as much as a factor of 2 in both the lateral and depth dimensions. However, as with all deconvolution procedures, this improvement in resolution comes at the expense of a degraded signal-to-noise ratio.

Among the advantages of CLEAN are its simplicity and flexibility. CLEAN permits restoration of images recorded by OCT imaging systems characterized by nonstationary PSFs. It tolerates speckle noise well and its performance degrades gracefully as the number of unresolvable scatterers causing mutual interference increases. Moreover, the quality of the restorations does not depend critically on the choice of input constants that control the convergence of the algorithm.

A drawback of the CLEAN algorithm is that it is too slow for use in real-time restoration of optical-coherence images on currently available personal computers. To reduce processing time, deconvolutions can be restricted to one dimension and the loop gain can be increased to reduce the number of iterations. However, both of these modifications reduce performance. An alternative method, which I employ in my own studies, is to deconvolve a small portion of the image inside a window centered on the feature of interest.

In this study I did not attempt to exploit the full potential of CLEAN. An approach that utilizes both the amplitude and phase information available in the interference signal deserves attention as a focus of future research. Rather than, as in this study, deconvolving the positive magnitude of the interference signal after envelope detection, it may be beneficial to deconvolve the raw ac interference signal using the coherent PSF as the CLEAN convolution kernel.[26] This approach would require sampling the interference signal at a frequency several times higher than the carrier (Doppler) frequency, while maintaining synchronization with a reliable phase reference. Success may lead to a solution of the inverse problem that embodies speckle reduction as a part of the deconvolution procedure.

Acknowledgment

I am pleased to acknowledge the partial funding of this work by the Research Grants Council of Hong Kong.

REFERENCES

1. B. Chance, ed., *Time-Resolved Spectroscopy and Imaging of Tissues, Proc. SPIE* **1431** (1991).
2. R. R. Alfano, ed., *Advances in Laser and Light Spectroscopy to Diagnose Cancer and Other Diseases, Proc. SPIE* **2135** (1994).

3. J. G. Fujimoto, M. E. Brezinski, G. J. Tearney, S. A. Boppart, B. Bouma, M. R. Hee, J. F. Southern, and E. A. Swanson, ''Optical biopsy and imaging using optical coherence tomography,'' *Nature Medicine* **1**, 970–972 (1995).
4. D. Huang, E. A. Swanson, C. P. Lin, J. S. Schuman, W. G. Stinson, W. Chang, M. R. Hee, T. Flotte, K. Gregory, C. A. Puliafito, and J. G. Fujimoto, ''Optical coherence tomography,'' *Science* **254**, 1178–1181 (1991).
5. C. K. Hitzenberger, W. Drexler, and A. F. Fercher, ''Measurement of corneal thickness by laser doppler interferometry,'' *Invest. Ophthalmol. Vis. Sci.* **33**, 98–103 (1992).
6. J. M. Schmitt, M. Yadlowsky, and R. F. Bonner, ''Subsurface imaging of living skin with optical coherence microscopy,'' *Dermatology* **191**, 93–98 (1995).
7. M. B. Brezinski, G. J. Tearney, B. E. Bouma, J. A. Izatt, M. R. Hee, E. A. Swanson, J. S. Southern, and J. G. Fujimoti, ''Optical coherence tomography for optical biopsy: properties and demonstration of vascular pathology,'' *Circulation* **93**, 1206–1213 (1995).
8. J. A. Izatt, M. D. Kulkarni, H. W. Wang, K. Kobayashi, and M. V. Sivak, ''Optical coherence tomography and microscopy in gastrointestinal tissues,'' *IEEE J. Selected Topics in Quantum Electron.* **4**, 1017–1028 (1996).
9. B. Bouma, G. J. Tearney, S. A. Boppart, M. R. Hee, M. E. Brezinski, and J. G. Fujimoto, ''High-resolution optical tomographic imaging using a modelocked Ti:Al_2O_3 laser source,'' *Opt. Lett.* **20**, 1486–1488 (1995).
10. J. M. Schmitt, S. L. Lee, and K. M. Yung, ''An optical coherence microscope with enhanced resolving power,'' *Opt. Commun.* **142**, 203–207 (1997).
11. J. M. Schmitt, ''Array detection for speckle reduction in optical coherence microscopy,'' *Phys. Med. Biol.* **42**, 1427–1439 (1997).
12. R. K. Tyson, *Principles of Adaptive Optics*, Academic Press, New York (1991).
13. J. M. Schmitt, A. Knüttel, M. Yadlowsky, and R. F. Bonner, ''Optical-coherence tomography of a dense tissue: statistics of attenuation and backscattering,'' *Phys. Med. Biol.* **39**, 1705–1720 (1994).
14. F. Forsberg, A. J. Healey, S. Leeman, and J. A. Jensen, ''Assessment of hybrid speckle reduction algorithms,'' *Phys. Med. Biol.* **36**, 1539–1549 (1991).
15. F. A. Sadjadi, ''Perspective on techniques for enhancing speckled imagery,'' *Opt. Eng.* **29**, 25–30 (1990).
16. M. D. Kulkarni and J. A. Izatt, ''Digital signal processing in optical coherence tomography,'' *Proc. SPIE* **2981** 2–6 (1997).
17. L. Zhou and J. M. Schmitt, ''Deconvolution and enhancement of optical coherence tomograms,'' *Proc. SPIE* **2981**, 46–57 (1997).
18. J. A. Högbom, ''Aperture synthesis with non-regular distribution of interferometer baselines,'' *Astron. Astrophys. Suppl.* **15**, 417–426 (1974).
19. T. J. Cornwell, ''A method for stabilizing the CLEAN algorithm,'' *Astron. Astrophys.* **121**, 281–285 (1983).
20. U. J. Schwartz, ''The reliability of CLEAN maps and the corrugation effect,'' in *Indirect Imaging*, J. A. Roberts, ed., pp. 255–260, Cambridge University Press, Cambridge (1984).
21. J. H. T. Bates, W. R. Fright, R. H. T. Bates, ''Wiener filtering and cleaning in a general image processing context,'' *Mon. Not. R. Astr. Soc.* **211**, 15–30 (1984).
22. P. W. Gorham, A. M. Ghez, C. A. Haniff, and T. A. Prince, ''Recovery of diffraction-limited object autocorrelations from astronomical speckle interferograms using the CLEAN algorithm,'' *Astron. J.* **100**, 294–306 (1990).
23. J. M. Schmitt and A. Knüttel, ''Model of optical coherence tomography of heterogeneous tissue,'' *J. Opt. Soc. Am. A* **14**, 1231–1242 (1997).
24. D. L. Fried, ''Analysis of the CLEAN algorithm and implications for superresolution,'' *J. Opt. Soc. Am. A* **12**, 853–860 (1995).
25. See, for example, R. N. Bracewell, *Two-Dimensional Imaging*, Ch. 13 and included references, Prentice-Hall, Englewood Cliffs, NJ (1995).
26. J. Tsao and B. D. Steinberg, ''Reduction of sidelobe and speckle artifacts in microwave imaging: the CLEAN technique,'' *IEEE Trans. Ant. Propag.* **36**, 543–546 (1988).